Calcium-dependent Inactivation Terminates Calcium Release in Skeletal Muscle of Amphibians

Eduardo Ríos,[1] Jingsong Zhou,[1] Gustavo Brum,[4] Bradley S. Launikonis,[3] and Michael D. Stern[2]

[1]Section of Cellular Signaling, Department of Molecular Biophysics and Physiology, Rush University, Chicago, IL 60612
[2]Laboratory of Cardiovascular Science, Gerontology Research Center, National Institute on Aging, Baltimore MD 21224
[3]School of Biomedical Sciences, University of Queensland, Brisbane, Queensland 4072, Australia
[4]Departamento de Biofísica, Universidad de la República, Facultad de Medicina, Montevideo 11800, Uruguay

In skeletal muscle of amphibians, the cell-wide cytosolic release of calcium that enables contraction in response to an action potential appears to be built of Ca^{2+} sparks. The mechanism that rapidly terminates this release was investigated by studying the termination of Ca^{2+} release underlying sparks. In groups of thousands of sparks occurring spontaneously in membrane-permeabilized frog muscle cells a complex relationship was found between amplitude *a* and rise time *T*, which in sparks corresponds to the active time of the underlying Ca^{2+} release. This relationship included a range of *T* where *a* paradoxically decreased with increasing *T*. Three different methods were used to estimate Ca^{2+} release flux in groups of sparks of different *T*. Using every method, it was found that *T* and flux were inversely correlated, roughly inversely proportional. A simple model in which release sources were inactivated by cytosolic Ca^{2+} was able to explain the relationship. The predictive value of the model, evaluated by analyzing the variance of spark amplitude, was found to be high when allowance was made for the out-of-focus error contribution to the total variance. This contribution was estimated using a theory of confocal scanning (Ríos, E., N. Shirokova, W.G. Kirsch, G. Pizarro, M.D. Stern, H. Cheng, and A. González. *Biophys. J.* 2001. 80:169–183), which was confirmed in the present work by simulated line scanning of simulated sparks. Considering these results and other available evidence it is concluded that Ca^{2+}-dependent inactivation, or CDI, provides the crucial mechanism for termination of sparks and cell-wide Ca^{2+} release in amphibians. Given the similarities in kinetics of release termination observed in cell-averaged records of amphibian and mammalian muscle, and in spite of differences in activation mechanisms, CDI is likely to play a central role in mammals as well. Trivially, an inverse proportionality between release flux and duration, in sparks or in global release of skeletal muscle, maintains constancy of the amount of released Ca^{2+}.

The Journal of General Physiology

INTRODUCTION

Skeletal muscle cells may contract and relax at frequencies of up to 200 Hz (e.g., Rome et al., 1996), which requires the messenger Ca^{2+} ions to undergo rapid cycling between cytosol and cell store. A requisite for this cycling is the nearly simultaneous and short-lived opening of Ca^{2+} release channels of the sarcoplasmic reticulum (SR). The opening of a large fraction of the channels occurs in response to a rapid conformational signal by the CaV1.1 voltage-sensing proteins of the transverse tubules, driven by the action potential. In the muscles of frogs and other amphibians, this conformational signal appears to be amplified by Ca^{2+}-dependent activation of channels not directly coupled to the voltage sensors (Pouvreau et al., 2007).

An equally concerted closing of the channels (Pape et al., 1993; Stern et al., 1997), which is complete and rarely followed by reopenings, follows upon membrane repolarization (Lacampagne et al., 2000). But, perhaps more interestingly, a rapid closure of release channels occurs in all species studied, even if the cell membrane remains depolarized (Baylor et al., 1983; Melzer et al., 1984). A spontaneous closure with similarly rapid kinetics (in the few milliseconds range) terminates Ca^{2+} release in Ca^{2+} sparks (Ríos et al., 1999; Lacampagne et al., 2000).

Kinetic similarity is but one of the pieces of evidence that Ca^{2+} sparks (for reviews see Baylor, 2005; Klein and Schneider, 2006) constitute elementary building blocks of physiological cell-wide (or global) Ca^{2+} release, or, in other words, that the initial peak of global release, crucial in the contractile response to action potentials, results from superposition of sparks. In support of this idea, first formally proposed by Klein et al. (1997), Pouvreau et al. (2007) have shown that both the production of sparks upon membrane depolarization and a cell-wide release evolution characterized by a large peak (relative to the steady level reached upon clamp depolarization) depend on the presence of ryanodine receptor 3 (RyR3), isoform 3 of the Ca^{2+} release channel of the sarcoplasmic reticulum. Also pointing in this direction are evidences that both sparks and a major portion of the cell-wide

Correspondence to E. Ríos: erios@rush.edu

Abbreviations used: CDI, Ca^{2+}-dependent inactivation; CICR, Ca^{2+}-induced Ca^{2+} release; FWHM, full width at half maximum; NA, numerical aperture; PSF, point spread function; RyR, ryanodine receptor.

peak require Ca^{2+}-induced opening of release channels, Ca^{2+}-induced Ca^{2+} release (CICR) (e.g., Jacquemond et al., 1991; Pizarro et al., 1992; Klein et al., 1996; Pape et al., 2002; Brum et al., 2003; Pouvreau et al., 2007).

For the above reasons it is widely believed that the mechanism or mechanisms determining channel closure and termination of Ca^{2+} release in sparks are also operative in the termination of global, physiological Ca^{2+} release.

In this paper we demonstrate a set of properties of Ca^{2+} release termination in sparks and then show that they are straightforwardly explained as the result of inhibition by Ca^{2+} acting on the cytosolic side of the RyR channels.

Put together with other evidence reviewed recently (Ríos et al., 2006), these results and conclusions suggest that termination of Ca^{2+} release in skeletal muscle is unlike that of cardiac muscle, where termination of Ca^{2+} sparks (elementary units of the cell-wide transients) is believed to largely depend on a signal caused by partial Ca^{2+} depletion in the SR, a signal perhaps conveyed through ancillary SR proteins like triadin and calsequestrin (Györke et al., 2002, Stern and Cheng, 2004).

MATERIALS AND METHODS

Ca^{2+} sparks were imaged at 17–20°C in saponin-permeabilized skeletal muscle fibers from *Rana pipiens* semitendinosus muscle. Adult frogs were killed by double pithing under anesthesia. Procedures were approved by Rush University's IACUC. Procedures and solutions for fiber dissection and mounting are published (Zhou et al., 2003). Data presented were obtained with two internal solutions: a "reference," with glutamate as main anion, and one with sulfate as main anion (a solution found to determine intriguing changes in spark morphology, e.g., Zhou et al., 2005), with compositions given in Zhou et al. (2003), Table I. Internal solutions had 100 µM fluo-4.

Line scans were obtained with two confocal scanning microscopes, an MRC 1000 (Bio-Rad Laboratories, Inc.) using a 40×, 1.2 NA water-immersion objective (Carl Zeiss MicroImaging, Inc.) or a SP2-AOBS with a 63× objective of the same NA (Leica Microsystems). The spatial width of the point spread function of these microscopes (full width at half maximum [FWHM] of Gaussian functions fitted to the profiles of the images of fluorescent beads of 0.1 µm diameter) were 0.47 and 1.44 µm (respectively in the focal *x*-*y* plane and the *z* direction) for the Carl Zeiss MicroImaging, Inc. miscoscope, and 0.47 and 0.89 µm for the Leica. Fluorescence $F(x, t)$ excited at 488 nm was determined at 2-, 1.875-, or 0.5-ms intervals and pixel distances given in the text, and normalized to its resting average $F_0(x)$. Sparks were located on a spatially filtered version of the normalized image as previously described (Zhou et al., 2003). Parameters measured on the unfiltered image for every event include the following: amplitude (peak minus local average before the event), FWHM (spatial width of the region exceeding half amplitude at the time of peak), and rise time (between 0.1 and peak, on a spline interpolate). That the determination of rise time is done on averages of spline interpolates of the three central pixels of sparks nominally increases the temporal resolution by a factor of 3 (González et al., 2000).

The signal mass M of events was calculated as a function of time t by text Eq. 2. (Chandler et al., 2003). Signal mass production rate was calculated numerically from M.

Ca^{2+} release flux underlying sparks was calculated by the so-called "backward" method developed by Blatter et al. (1997) and Ríos et al. (1999). In brief, the evolution $[Ca^{2+}]$ (x, t) is first derived from the fluorescence in spark averages by solving suitable diffusion–reaction equations. The $[Ca^{2+}]$ waveform, assumed to be spherically symmetric, is then used to calculate reaction and diffusion fluxes of Ca^{2+} due to known ligands and removal mechanisms. Release flux density is derived as sum of these components plus the local Ca^{2+} concentration change, while total flux and the proportional release current are calculated by volume integration of the density in the region where it is positive. Specifically, dynamical variables were Diffusible: $[Ca^{2+}]$, [Fluo3], [CaFluo3], [EGTA], [CaEGTA], $[SO_4^{2-}]$, $[CaSO_4]$, [ATP], [CaATP], [MgATP], [PV] (parvalbumin), [CaPV], [MgPV]; and Fixed: [CaTNC], [Fluo3Protein], [CaFluo3Protein], [CaSERCA], SERCA transport. Reaction and diffusion calculations use conventional parameter values listed in Table I of Ríos et al. (1999). Note that the calculation does not involve "deblurring" (correction for the blurring of sparks by the imaging system). As shown in prior work (Ríos et al., 1999), deblurring for the point spread function (PSF) measured in our Carl Zeiss MicroImaging, Inc. system (FWHM of 0.47 and 1.44 µm) results in an increase in calculated release current by close to twofold. Because deblurring greatly increases noise, we chose not to use it and instead introduce a correction factor ϕ (defined in Eq. 8) when comparing simulated and experimental sparks.

Spark Simulations

Skeletal muscle calcium sparks were simulated by solving a system of reaction–diffusion equations describing the movement and interaction of calcium with a complete system of skeletal muscle intracellular calcium buffers, as described in Ríos et al. (1999). The dynamic variables were the same used for the backward calculation of flux. Reaction–diffusion equations were discretized into 100 concentric spherical shells of thickness 30 nm each with the spark source calcium represented as a rectangular pulse of calcium current deposited uniformly in a central sphere of radius 100 nm. This converted the problem to a system of 1,300 ordinary differential equations that were solved using the modeling system FACSIMILE. For each spark, a simulated confocal line scan was generated by convolving the fluorescence of free and bound fluo-3 with the empirically measured PSF (Ríos et al., 1999) of the confocal microscope, positioned along an x-axis line offset from the center of the spark by randomly chosen y-axis and *z*-axis displacements uniformly distributed within an ellipse of major axes 4 µm (y) and 6 µm (z). For each randomly chosen offset, convolution integrals were calculated using nested calls to a Gauss-Kronrod integration routine written in Fortran to generate a 29 × 100 "blurring matrix" mapping spherical shells of fluo-3 onto 29 pixels along the scan line. The amplitude (peak $\Delta F/F_0$) and rise time of the simulated spark image were then estimated from a spline interpolation onto a 20-fold finer time step, as was done with the experimental data. For the purposes of this study, the effects of microscope photon noise were not included, since the presence of noise makes the results dependent on the details of the spark detection algorithm, a complicated image processing routine written in IDL with many features for rejecting false positive sparks in experimental line scans. Instead, simulated sparks were "detected" simply by including only those sparks with amplitude >0.3. In this way, we were able to restrict ourselves to the statistical features that are a direct consequence of the random offset of sparks from the scan line. That the essential aspects of the randomization of amplitudes derived from the scanning process is well captured by this simulation was confirmed by the good agreement between experimentally measured amplitude variance and its value in the simulation.

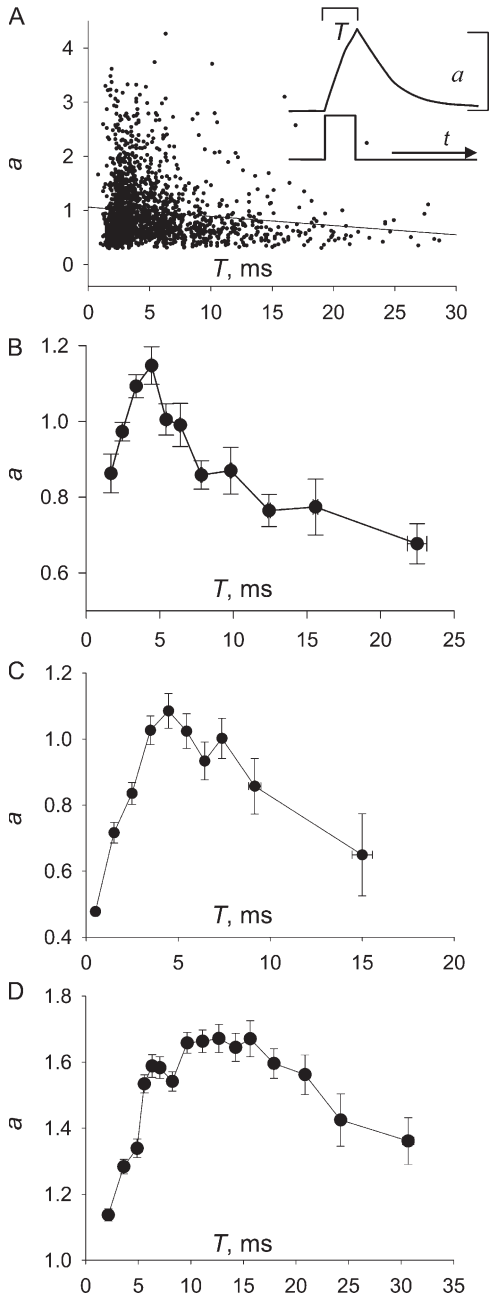

Figure 1. The relationship between spark rise time and amplitude. (A) Rise time, *T*, vs. amplitude, *a*, of 1,887 sparks collected in 700 images of seven frog fibers with permeabilized membrane, placed in standard glutamate solution. Fibers were imaged at 0.135 µm per pixel and 2 ms per line. Sparks were detected and parameters were measured automatically on an interpolated average of three central pixels. Correlation coefficient $r^2 = 0.015$, regression coefficient $b = -0.017$ ms^{-1}. Inset: top, schematic of the profile F/F_0 vs. t at the spatial center of the spark, indicating a and T; bottom, Ca^{2+} flux during spark is thought to be roughly constant and last for the rise time. (B) Average a vs. average T in "bins" of increasing T for the group of sparks in A. Bars represent ± SEM of a and T. (C) Average a vs. average T, determined as described for B, for a set of 881 sparks detected in 500 images of two frog fibers imaged at 0.14 µm per pixel and 0.5 ms per line. (D) Average a vs. T, for a set of 6,300 sparks in 1,000 images of four permeabilized fibers placed in sulfate-based solution and imaged at 0.23 µm per pixel and 1.875 ms per line.

The simulations aimed on one hand to test whether and how different models of spark release current and/or duration affected the distribution of amplitudes and rise times determined in line scans, thus testing whether experimental distributions could be used to evaluate such models. A second purpose of the simulations was to test predictions (about these amplitude distributions) derived from a theory of confocal scanning (Ríos et al., 2001). For the first goal, two distributions of parameters were used, with results represented in Fig. 5. To represent sparks satisfying the calcium inactivation model of Scheme 1, release durations were randomly assigned according to an exponential distribution with a mean of 5 ms. Release current m_3 was then calculated for each spark from its release duration T by approximate numerical inversion of Eq. 6 subject to an upper bound ($m_3 = 40$ pA*(2.163 ms/$T - 0.061$); $m_3 \leq 37$ pA). Then, to generate a comparable representation of a "null model," another set of simulated sparks was generated with a distribution of release current duration that was the same as in the calcium inactivation model, but with constant release current.

The simulations done to test the theory of line scanning are described in the Appendix. To examine the pure effect of scan line offset on the distribution of apparent spark amplitudes, a population of sparks with random offsets from the scanned line, but fixed source current and duration, was generated. This study is illustrated with Fig. A1. To test the ability of theory to recover the "true amplitude" distribution of a set of sparks from the distribution of amplitudes measured in line scans, a large set of simulated sparks was generated with three different values of release current and release duration. The results of these are presented in Figs. A2 and A3.

Because of the large amount of computation required to carry out the convolution integrals, simulations were performed simultaneously on 160 AMD Opteron processors in the high performance Biowulf Linux cluster at the National Institutes of Health (http://biowulf.nih.gov).

RESULTS AND DISCUSSION

In this section we analyze quantitative "morphometric" properties of large sets of sparks imaged in frog fast twitch muscle and demonstrate a paradoxical relationship between two of these properties, amplitude (a) and rise time (T). Then we develop a simple theory of Ca^{2+}-dependent inactivation, which accounts for the main observations.

The inset of Fig. 1 A represents diagrammatically the fluorescence profile (top trace) and the Ca^{2+} current (or release flux, bottom) believed to underlie a Ca^{2+} spark (evidences for this view are summarized by Baylor, 2005, and Klein and Schneider, 2006). Ca^{2+} current starts abruptly and remains approximately constant, as far as the temporal resolution of various methods can tell, until it terminates, abruptly as well. The time of active release has been shown with simulations to match fairly well the spark rise time T (elapsed from start to peak fluorescence), even for off-focus sparks (e.g., Pratusevich and Balke, 1996; Jiang et al., 1999).

Even if the rate of rise of the fluorescence is not constant during the time of active release, a straightforward

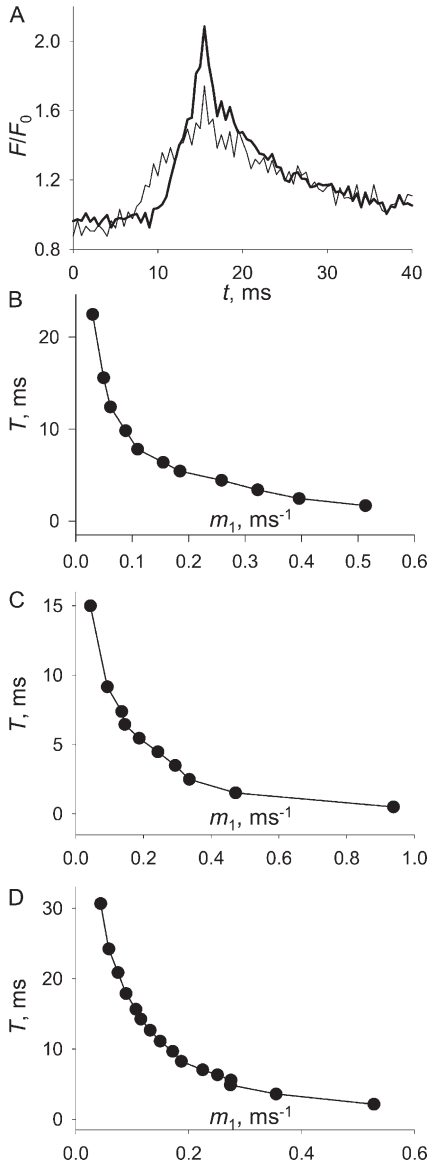

Figure 2. The relationship between rise time and a simple estimator of Ca^{2+} release flux in sparks. (A) Examples of spark profiles used to estimate release flux. Thick trace, F/F_0 vs. t at the center of the average of the 88 sparks with T between 4 and 5 ms in the group represented in Fig. 1 C. Thin trace, F/F_0 vs. t for the average of the 18 sparks with T between 9 and 11 ms in the same group. Release flux was estimated by the average rate of rise of normalized fluorescence, m_1, calculated on bin averages as the ratio a/T, which for the averages shown is respectively 0.234 and 0.069 ms^{-1}. Note that the time-varying rate of rise of fluorescence may diverge substantially from m_1. (B–D) Bin averages of T plotted against m_1 for the sets of sparks in Fig. 1, B–D. A similar, strictly monotonic dependence is obtained in all cases.

expectation from this simple picture is that longer-lasting Ca^{2+} release (i.e., longer T) should result in sparks of greater amplitude. Simulations discussed later confirm this prediction for sparks of the same, constant flux. In contrast, the experimental data do not fulfill this expectation.

The Relationship between Spark Amplitude and Rise Time

Fig. 1 A plots a vs. T for a set of 1,886 sparks occurring spontaneously in frog semitendinosus fibers with the plasma membrane permeabilized by saponin. The frequency of occurrence of these sparks was increased to $\sim$6 s^{-1} (100 μm)$^{-1}$ (or $\sim$0.2 s^{-1} per sarcomere) by reducing $[Mg^{2+}]$ in the cytosolic solution to 0.4 mM. Plots with similar properties were obtained from a set of $\sim$900 sparks also imaged in membrane-permeabilized frog muscle cells, but at an acquisition rate of 0.5 ms/line and an additional set of 6,300 events, in a cytosolic solution with sulfate instead of glutamate as main anion. A plot with nearly identical properties has been published for sparks elicited by low voltage depolarization in cut segments of frog fibers with intact plasmalemma (Ríos et al., 1999, Fig. 5 C). The main features of the relationship therefore do not depend on stimuli or conditions of acquisition, to the extent that these were varied.

The scatter plot in Fig. 1 A shows a poor correlation between amplitude and rise time. The first order regression line had negative slope and a barely significant correlation coefficient. As argued below, the poor correlation largely reflects the variation in apparent spark amplitude due to variation in the distance between spark source and confocal scan line.

A more elaborate analysis, represented in the other panels of Fig. 1, unveiled more features in the relationship. Sparks were separated according to rise time, grouped in unequal "bins" that were chosen for rough equality of events per bin. Plotted in Fig. 1 B are average a vs. average T in each bin for the set of sparks of panel A. Bidirectional bars represent one standard error on each side of the mean. Naturally, average values of T were close to the center of each bin.

The analysis reveals clearly a relationship with two regions: at T of 4.5 ms or less the amplitude increases with T. It is only at T greater than 4.5 that the paradoxical decreasing relationship is found. These features appeared independently of the choice of binning intervals.

Panels C and D demonstrate qualitatively similar properties in the group of sparks imaged at a higher scanning rate and in the set obtained in sulfate solution (though in the latter the maximum is clearly displaced to a greater T).

The analysis therefore improves upon the simple linear regression, in revealing two regions of rise time where two strong correlations of opposite sign exist. Unexpected relationships between amplitude and rise time have been noticed before: Lacampagne et al. (1999) found similarity of amplitudes among groups of sparks of different T imaged with a fast scanner (a result not inconsistent with the present one, considering the much smaller number of events and range of T values covered in the study cited). Likewise, in their study of cardiac myocyte sparks with quantized rates of fluorescence rise, Wang et al. (2004) noticed an inverse

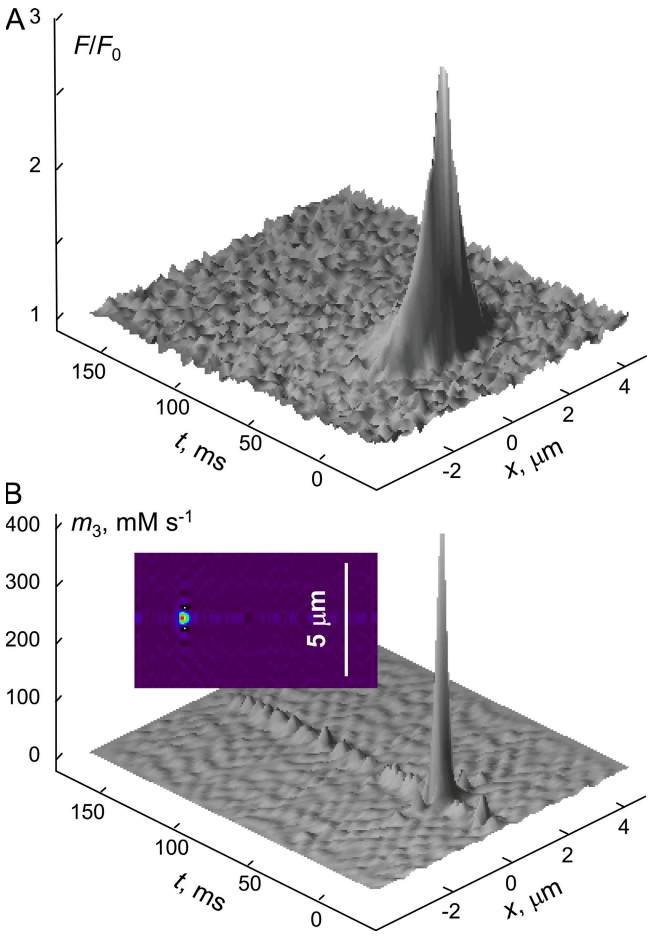

Figure 3. Ca^{2+} release flux calculated ab initio. (A) Average of fluorescence in all sparks with T between 4 and 5 ms in the group represented in Fig. 1 A. (B) Release flux density calculated from the average in A, by the "backward" algorithm (details in Materials and methods). The inset is an *x-y* projection that shows well the narrow footprint of the calculated flux.

correlation between number of quanta (which mapped to greater a) and T.

Ca^{2+} Flux and Spark Rise Time Are Related Inversely

A simple transformation of the data presents this relationship in a simpler and more meaningful form. The transformation is based on the assumption of near proportionality between Ca^{2+} release flux and rate of change of fluorescence, in sparks as well as global signals. As examples of data used for this calculation, Fig. 2 A shows the profile of normalized fluorescence F/F_0 of averages of two groups of sparks from the set represented in Fig. 1 C. The profile in thick trace is from sparks with T between 4 and 5 ms, while that in thin trace is from sparks with T between 9 and 11 ms. An average rate of rise of fluorescence during the time of Ca^{2+} release is calculated as the ratio of amplitude by rise time and represented by m_1.

$$m_1 \equiv a / T \tag{1}$$

The results of this calculation applied to all datasets in Fig. 1 are represented in Fig. 2 (B–D). T is represented on the ordinate axis to emphasize the conclusion, reached eventually, that T is largely determined by the value of flux.

It is clear from inspection that this operation on the data uncovers a simple, monotonically decaying relationship between rise time and a proxy for Ca^{2+} flux.

The estimation of flux represented by Eq. 1 is coarse however. One limitation can be appreciated in the profiles of fluorescence in Fig. 2 A. Because the rate of rise varies as a function of time, its average during the rise time may seriously underestimate the maximum. Also, as will be demonstrated later with simulated sparks, amplitude associated with a constant flux tends to a saturation value as release duration increases. Moreover, because the transformation involves explicit division by T, it comes as no surprise that the resulting ratio m_1 should decay with increasing T.

To overcome these weaknesses, two additional estimations of release flux were used, none of which involved explicit division by T. One approximated release flux as the rate of change of signal mass, or spark mass, M. Following Chandler et al. (2003), M was calculated assuming that sparks are spherically symmetric, as

$$M(t) \sim 1.206 \frac{\Delta F}{F_0}(t, x = 0)\, FWHM(t)^3. \tag{2}$$

In this equation fluorescence F and its initial value F_0 are evaluated on the spark averages at each bin of rise time at the location x of the spark peak; FWHM (t) represents the full width at half maximum of $\Delta F(t,x)$, calculated from the Gaussian standard deviation σ of the spatial profile at time t as $2(2\ln 2)^{0.5}\sigma$. Peak rate of change, calculated on M (t), was close in value to its average over the duration of the rising phase of $M(t)$. This average was calculated for all bins of T in the set of sparks represented in Fig. 1 (A and B). Denoted as m_2, it is plotted against T by green symbols in Fig. 4. In the same figure, m_1, calculated by Eq. 1, is represented in black.

The third approach was to explicitly calculate release flux from the time course of the averaged sparks, by the ab initio "backward" method of Ríos et al. (1999). This calculation was performed for the averages of sparks in bins of different T from the set in Fig. 1 A. The average of sparks and the calculated release flux density are illustrated for the bin of rise time 4–5 ms, in Fig. 3. The flux is calculated as the sum of removal by ligands and transporters, diffusion away from the source, and rate of change of the local concentration. These terms are all driven by $[Ca^{2+}]$ (x,t), which is derived from the measured $F(x,t)$ (Fig. 3 A) using the known binding kinetics and diffusion properties of the monitoring Ca^{2+} sensor. The calculation yields a flux density (with dimensions of concentration

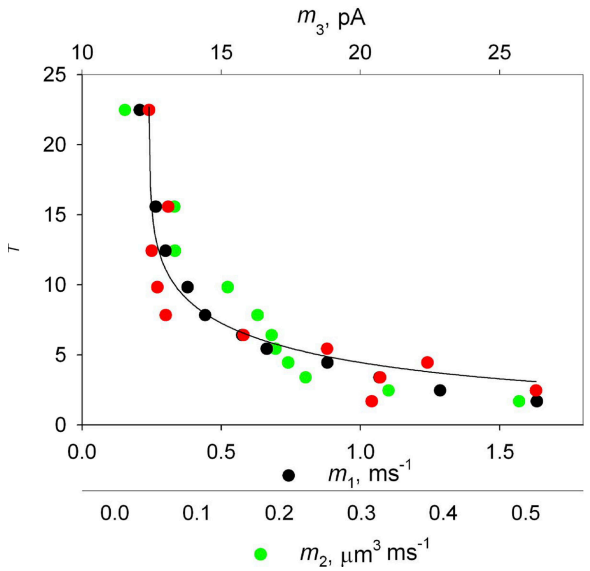

Figure 4. Rise time vs. different estimators of release flux. Black symbols, T vs. m_1, calculated from binned averages in Fig. 1 B by Eq. 1 (same values as in graph in Fig. 2 B). Green, T vs. m_2, calculated according to Eq. 2 for the same spark averages. Red, T vs. m_3, release current calculated by volume integration of flux density derived for the same spark averages by the backward method. Continuous curve, best fit to T vs. m_3 by Eq. 6. Best fit parameters: $k_i\beta$, 2.3 mM^{-1}; k_r, 0.061 ms^{-1}; A^* = 0.115.

change per unit time) as a function of time and space (Fig. 3 B). The flux density obtained by this calculation, integrated over volume at the time of its maximum and converted proportionally to intensity of Ca^{2+} release current is denoted as m_3 and plotted in red in Fig. 4.

m_1, m_2, and m_3 all exhibit a similar dependence with T. The approximate inverse relationship between Ca^{2+} flux and rise time therefore applies robustly, independently of the approach used to estimate flux.

A Ca^{2+}-dependent Inactivation Model of Spark Termination

An inverse relationship between ion flux and rise time (i.e., channel open time) is to be expected whenever the permeant ion, acting on the exit side, is able to inactivate, inhibit, or by any means close the channel. In the following the term "inactivation" is used to underscore a presumption that the resulting channel closure is independent of activation processes that may act elsewhere on the channels.

The idea of a Ca^{2+}-dependent inactivation can be formalized by first noting that the local $[Ca^{2+}]$ increase at the exit site, i.e., at the putative inhibitory site on the channels, should be proportional to the flux, provided that the geometry of the source is not different in sparks of different flux (e.g., Ríos and Pizarro, 1991; Jong et al., 1995). Namely

$$[Ca^{2+}]_{local} = \beta m, \qquad (3)$$

where β is a constant that depends on physical aspects of the medium and geometry of the "local" site. We used Eqs. 1 and 3 to derive predictions from the model in Scheme 1, a two-state model of the spark Ca^{2+} source (a cluster of channels) that leaves unspecified all geometric details.

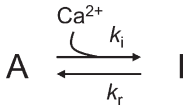

(SCHEME 1)

To account for the observation of an approximately constant flux during the spark rise time, the source is assumed to be capable of just two flux values, m or zero. In every spark, channels start in state A (available) and undergo a continuous transition to state I (inactivated), driven by the local Ca^{2+} increase calculated from Eqs. 1 and 2. Let $A(t)$ represent the evolution of the occupancy of state A, this evolution is determined by

$$dA/dt = -k_i \beta m A + (1 - A)k_r. \qquad (4)$$

Because m is assumed to be constant, the occupancy A undergoes an exponentially time-dependent decay

$$A = \frac{k_r}{k_i \beta m + k_r} + \frac{k_i \beta m}{k_i \beta m + k_r} e^{-(k_i \beta m + k_r)t}, \qquad (5)$$

where t is measured from the beginning of the spark, at which point the value of A is one.

It is assumed that when A declines to a critical level, A^*, the source closes. Hence the time at which the level A^* is reached is equal to the release (open) time, Ξ, which is for practical purposes the rise time T. Solving Eq. 5 for T:

$$T = \frac{\ln(k_i \beta m) - \ln[A^* k_i \beta m - (1 - A^*)k_r]}{k_i \beta m + k_r}. \qquad (6)$$

Eq. 6 represents the model prediction for the relationship between T and m. The curve in Fig. 4 represents the best fit by Eq. 6 to the T vs. m_3 data (red) with adjustable parameters A^*, $k_i\beta$, and k_r at values listed in the figure legend. As should be obvious by inspection, reasonable fits are also possible for the two other evaluations of flux (m_1 and m_2).

The Model Predicts Spark Amplitude

While the model reproduces well the relationship between rise time and release current calculated from spark averages, a more direct test is whether it can predict measured spark amplitudes.

Note first that the model, via Eq. 6, defines an invertible relationship between T and m, while the ab initio or backward algorithm yields m (specifically m_3) starting from observed sparks (the parameters of which include a). In other words, we have methods to go from a to m, and

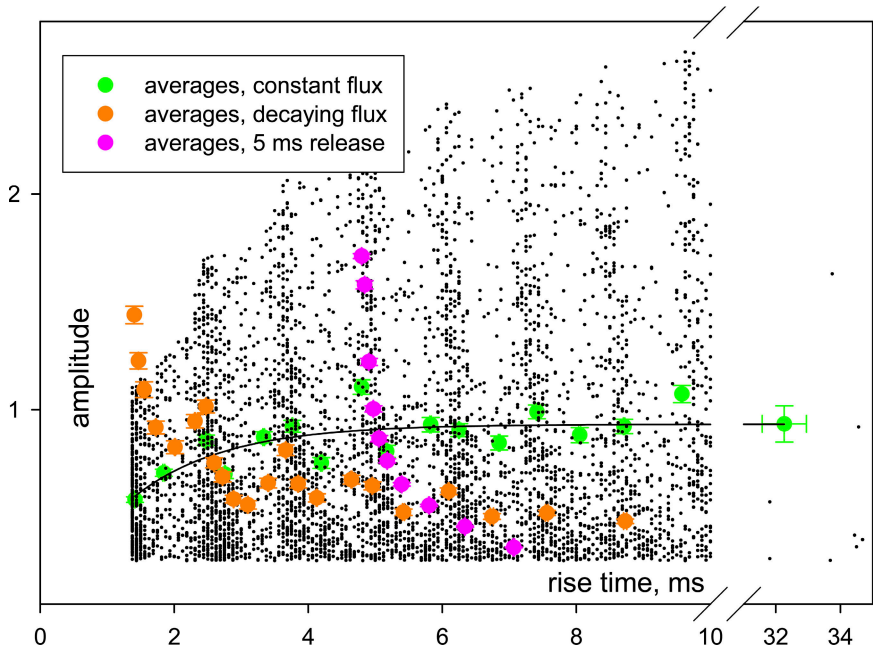

Figure 5. Amplitudes and rise times of simulated sparks. Dots plot detected amplitude, a_s vs. rise time in the line scan, T, for sparks generated at random locations in the simulation volume, using a current of 30 pA and release durations Ξ between 0.5 and 35 ms. The sparks represented had $a_s > 0.3$. Green circles, average values (±SEM) in bins of T containing 300 sparks each. Line, single exponential fit to bin averages (Eq. 7, with $b = 0.9409$ and $k = 0.7337$ ms^{-1}). Note that for sparks of constant release flux amplitude increases with T in a saturating manner. Pink symbols, bin averages of a_s for a set of 8,000 sparks simulated with current of 30 pA and $\Xi = 5$ ms. Note that while Ξ is constant, T varies in a narrow range, being in most cases greater than Ξ. Orange circles, bin averages of a_s of a set of 4,667 sparks simulated assuming the inverse relationship between Ξ and m_3. (Ξ was exponentially distributed, with a minimum of 0.5 ms. m_3 was calculated from Ξ by an approximate solution of Eq. 6 and $\Xi \sim T$). Note that the dependence between averaged amplitude and T reflects well the inverse relationship between flux and release time assumed in the simulation.

then from m to T. Predicting a requires inverting these two operations, which was done as follows: for each value of m_3 the corresponding T was obtained using Eq. 6. Then the backward algorithm was inverted in a "forward" calculation, a simulation that starting from flux yields a spark. Of course the simulation copied the "removal" properties of the medium that were assumed in the backward calculation of m_3.

The aim of the simulation was twofold: to generate a spark, a distribution of fluorescent Ca-bound dye and associated variables, given a flux and its duration, and to reproduce the deformations or "errors" intrinsic to confocal line scanning, namely the blurring of sparks scanned in focus and the further reduction in intensity and other deformations of sparks that originate away from the line of scanning. The errors were reproduced by placing large numbers of simulated sparks at random y and z distances from the scanning line (or x axis in spark space), and convolving with the experimentally determined PSF of the scanner. This was done for the time range of interest, to generate line scans that were then analyzed to determine a, T, and other morphological parameters. We denote as a_s the amplitude measured on the simulated line scans, which is less or equal than the amplitude measured on sparks scanned in-focus. a_s corresponds in the simulation to a observed in the experiments. When considering models and simulations we will also need to distinguish between Ξ, the release duration or source open time, and its close experimental measure, rise time T.

Fig. 5 represents with dots a_s vs. T for 6,665 sparks from a total of 20,000 that were placed at random locations in the simulation space. The sparks were generated with a current of 30 pA and Ξ exponentially distributed between 0.5 and 35 ms. The simulation volume was made sufficiently large for a_s to vary from a maximum (the in-focus value) to zero; the 6,665 sparks represented are those for which a_s is greater than the detectability criterion used in the experimental measurement (0.3). (The quasi periodic clustering of T of simulated sparks is a consequence of "sampling" the simulated fluorescence at the confocal line scan interval, a procedure detailed in Materials and methods. Such sample-rate periodicity is less conspicuous in the experimental data, probably due to the effects of photon noise. No significance is attached to this apparent periodicity.)

The green circles plot averaged a_s (±SEM) in 23 bins of T containing ~300 events each. The pink circles plot bin averages of a second, related set, in this case of 8,000 sparks simulated with a 30-pA current and a single release duration, 5 ms. Finally, the orange circles plot bin averages of 4,667 sparks simulated assuming the inverse relationship between release time and m_3 given by Eq. 6. It is obvious from these plots that simulated line scanning readily distinguishes the three types of dependence.

It is interesting that averaged scanned amplitudes of sparks generated with a single current and release time (pink symbols) decrease monotonically with T. While

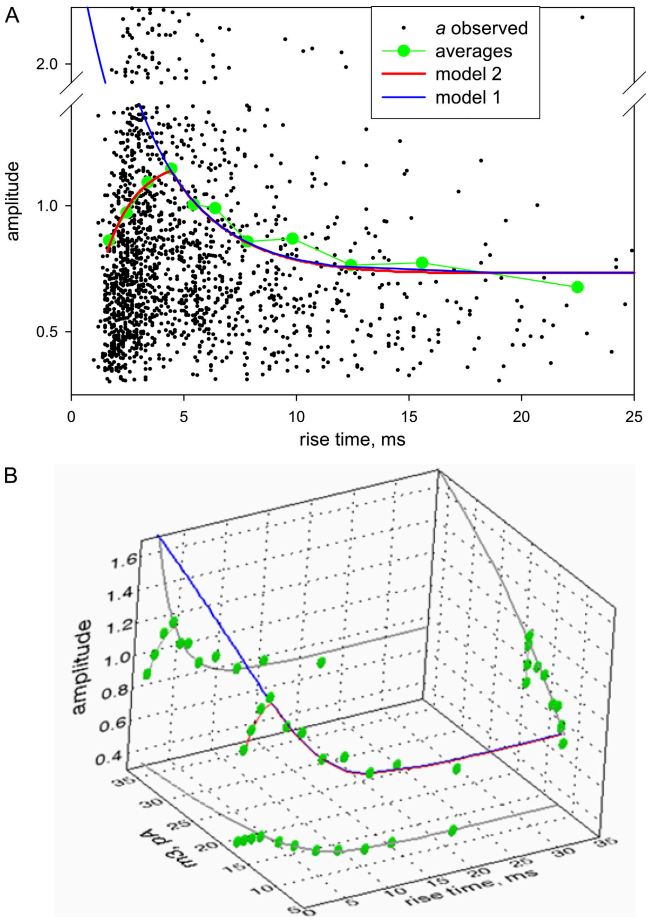

Figure 6. Model prediction of spark amplitudes. A, dots represent a vs. T for the first set of experimental sparks (as in Fig. 1 A). Circles represent their bin averages (as in Fig. 1 B). The curve in blue plots a as a function of T, calculated with "model 1," that is, Eqs. 9 and 6, with parameter values given in the legends of Figs. 4 and 5. The curve in red is by "model 2," for which m_3 is assumed constant (37 pA) at $T < 4.4$ ms. Note that in this range of T the $a(T)$ dependence is exponential, given by Eq. 7 scaled by 37/30. (B) Bin-averaged experimental a (circles), prediction by models 1 (blue line) and 2 (red), plotted as a function of both T (as in A) and m_3. The plot illustrates the model calculation of a, which relies on the bijective correspondence between T and m_3 given by Eq. 6.

neither the narrow range nor the steepness of this dependence can mimic the experimental values, the existence of a range in the abscissa confirms that T is a close but not entirely equivalent measure of release time, while the decreasing relationship indicates that sparks that are farther away from the scan line will systematically give rise to longer T in the line scan image.

As expected, the set with constant current and variable release time yields amplitude averages that increase with T. The continuous line represents a best exponential fit to the bin averages of this set. This exponential reproduces in a scaled-down version the clear dependence that exists between T and the maximum of a_s (the amplitude of sparks in-focus).

This curve (with parameters listed in the figure legend) summarizes the relationship expected between T and a for observed sparks of the same flux but variable release time. Representing the functional dependence that links spark amplitude to the two main simulation parameters by $a_s(\Xi, m_3)$, which is approximately equal to $a_s(T, m_3)$, then the exponential function in Fig. 5 is $a_s(T, 30\ \text{pA})$, namely:

$$a_s(T, 30\,pA) = be^{-kT}. \tag{7}$$

Assuming that a is proportional to m_3, a can be predicted for every m_3 by

$$a_s(T(m_3), m_3) = \frac{\phi m_3}{30} be^{-kT(m_3)}, \tag{8}$$

with $T(m_3)$ given by Eq. 6. ϕ is a factor, greater than 1, necessary to correct for the blurring of experimentally detected sparks associated to the imaging system. The value of ϕ required for best fit is 1.9, but a similar value was calculated using the PSF of our imaging system (Fig. 4; Ríos et al., 1999).

Fig. 6 A reproduces the scatter plot (a vs. T) of all events in Fig. 1 A, plus the bin averages of Fig. 1 B. In blue is the predicted amplitude, computed using Eq. 8, that is

$$a_s(T, m_3(T)) = \frac{\phi m_3(T)}{30} be^{-kT}, \tag{9}$$

where $m_3(T)$ is the functional inverse of Eq. 6, obtained numerically, and ϕ, 1.9, was determined for best fit of the decaying portion of the bin-averaged plot. It should be clear at this point that the model (named "model 1") reproduces well the observed a vs. T, but only in the range where this relationship is decreasing. Clearly, model 1 does not work at lower values of T.

A simple justification of the error results from examining the underlying dependence on release current, m_3. m_3 is a parameter in Eq. 9, explicitly displayed in Fig. 6 B as a curve in (T, m_3, a_s) space. m_3 varies between 12.4 pA at the highest values of T and 154 pA at the lowest. ϕ m_3, which more accurately corresponds to the release current, reaches 294 pA. Considering that these currents originate from a finite group of channels probably limited to one couplon (Stern et al., 1997), there must be an upper limit to the release current. Specifically, the increase of a with T that occurs at brief T up to a certain T_p may reflect the dependence when current is maximal, at a value corresponding to the activation of the full cluster of channels. Such modification, "model 2," is implemented by imposing the condition $m_3(T) = m_3(T_p)$ at all $T < T_p$. In the example, T_p is 4.4 ms and ϕ $m_3(T_p)$ = 37.0 pA. The prediction, calculated through Eq. 9 but using a constant m_3 at $T < T_p$ is represented in red in Fig. 6. Fig. 6 B displays clearly the modified

dependence of m_3 on T. Model 2 fits the data; and interestingly, 37 pA is a reasonable upper bound of current from arrays that may include one or two couplons, i.e., 60 or 120 channels (Franzini-Armstrong et al., 1999), each contributing 0.35–0.5 pA (Kettlun et al., 2003).

Explanatory Power of the CDI Model

While this analysis implies that a Ca^{2+}-driven inactivation (CDI) contributes to the termination of Ca^{2+} sparks, and by extension Ca^{2+} release at the cell-wide level, it does not tell how important this contribution is. The question was addressed by examining the reduction in variance of a achieved by subtracting the model prediction.

The total variance of the distribution of amplitudes in the set of 1,900 sparks of Fig. 1 A, i.e., $\langle (a - \bar{a})^2 \rangle$, where angle brackets represent expected value and $\bar{a} = \langle a \rangle$, was 0.344. This was compared with the unexplained variance, that of the difference between measured amplitude and amplitude predicted by the model, i.e., $\langle (a - a_s)^2 \rangle$.

Using model 2, the variance of $a - a_s$ was 0.316; in other words, the model only explained 7.8% of the variance in spark amplitudes. While this explaining power appears meager, additional considerations change this impression. First, the averages of a in successive bins of T (in green in Fig. 6) provide a maximum explanatory power of the a vs. T dependence in a,T space, as these bin averages are the values that minimize the squared deviation from all the points in the set. The a_s vs. T dependence, in red, does not differ from the averages in any systematic way. Indeed, the mean square deviation from the bin averages is 0.317; in other words, the explanatory power of model 2 is as good as can be for a one-dimensional model (one assuming that the spark is determined by only one independent variable, T, which is bijectively linked to m_3, in this case).

Understanding the explanatory power of the model also requires considering the contribution of out-of-focus errors to the total variance. Indeed, among spark parameters, amplitude is the one most sensitive to these errors. A very large part of the variance is due to the unknown separation between spark source and line of scanning.

Our theory of confocal sampling (Ríos et al., 2001), directly tested with simulations in the Appendix, makes it possible to evaluate the out-of-focus contribution to the variance in a. Let α be the measured in-focus amplitude of a set of identical sparks originated at random distances y and z from the scanning line; then, as demonstrated in Appendix 1 of Ríos et al. (2001), the measured amplitudes a are distributed according to

$$f(a) = \frac{n 2\pi\sigma^2}{a} \text{ for all } a \le \alpha, \tag{10}$$

where f is the density (number of sparks per unit length of scanning with amplitude in the interval a, $a + da$), n is total number of sparks per unit volume, and σ is the standard deviation of the point spread function of the microscope, assumed to be Gaussian and symmetric. This function is valid between the minimum detectable amplitude $a_{\min}$, and the full in-focus amplitude α. With the distribution in hand (Eq. 10) it is possible to calculate the expected value of a

$$\bar{a} = \frac{\int_{a_{\min}}^{\alpha} da}{\int_{a_{\min}}^{\alpha} \frac{1}{a} da} = \frac{\alpha - a_{\min}}{\ln\alpha - \ln a_{\min}} \equiv \frac{\Delta a}{Y}, \tag{11}$$

where $\Delta a = \alpha - a_{\min}$ and $Y = \ln\alpha - \ln a_{\min}$. The variance is

$$\sigma^2 = \frac{\int_{a_{\min}}^{\alpha} \frac{(a-\bar{a})^2}{a} da}{\int_{a_{\min}}^{\alpha} \frac{1}{a} da} = \frac{1}{Y^3} \int_{a_{\min}}^{\alpha} \frac{Y^2 a^2 - 2Ya\Delta a + \Delta a^2}{a} da = \tag{12}$$

$$= \frac{\alpha^2 - a_{\min}{}^2}{2Y} - \frac{(\Delta a)^2}{Y^2}.$$

While Eq. 12 was derived for a population of sparks of homogeneous amplitude, it can be shown numerically that the variance due to focusing error for groups of sparks of different in-focus amplitudes will have the same value as that of a homogeneous population, with single intermediate amplitude. Take the group of 1,900 sparks in Fig. 1 A; the mean value of their measured amplitude is 0.98. According to confocal sampling theory (Ríos et al., 2001), the in-focus amplitude α of a spark is 2–2.5 times its average measured value, hence the variance in amplitude due to out-of-focus error can be estimated applying Eq. 12 with $\alpha = 0.98 \times 2.25$ (or 2.2) and $a_{\min} = 0.3$ (as defined by the detection algorithm). The result is 0.285, quite close to the unexplained variance (0.316). This estimate demonstrates that the component due to out-of-focus errors is by far the largest fraction of the total variance. In this light, the predictive power of the theory resulting in Eq. 6, and hence the contribution of CDI to spark termination, appears to be much more significant.

As shown before (Pape et al., 1995; Rengifo et al., 2002) open channels beyond those in the Ca^{2+} source can contribute significantly to the local $[Ca^{2+}]$, which during the peak of a cell-wide transient may therefore increase beyond the level of the immediate source and render CDI more effective. (Addition of Ca^{2+} domains beyond spark boundaries of course negates the view of sparks as truly independent building blocks of the cell-wide signal. Based on multiple lines of evidence, others

have argued that a strictly "autonomic" view of sparks cannot be maintained anyway (e.g., Brum et al., 2003)).

Other Candidate Mechanisms of Release Termination

The dearth of other candidate mechanisms is consistent with our conclusion that the role of CDI is crucial in termination of Ca^{2+} release. In cardiac muscle, where most, if not all, of the Ca^{2+} release necessary for contraction occurs in the form of sparks, the termination of Ca^{2+} release is "timed" or synchronized (i.e., not Markovian, see for instance Wang et al., 2002) and this synchronization results, to a large extent, from depletion of Ca^{2+} in the SR (for reviews see Györke et al., 2002; Stern and Cheng, 2004). We recently reviewed the evidence for a similar mechanism in skeletal muscle (Ríos et al., 2006) and concluded that only experiments with release channels reconstituted in bilayers (Beard et al., 2002, 2005; Wei et al., 2006) showed clear effects of Ca^{2+}, acting from the SR side, on gating of the channels. When studied in living cells instead, the effects were either absent (Launikonis et al., 2006a) or occurred in the wrong direction (depletion caused an increase in Ca^{2+} release permeability) explicable by a cytosolic locus of (inhibitory) action by the Ca^{2+} that flows through the channels (Jong et al., 1993). Moreover, the actual reduction in $[Ca^{2+}]_{SR}$ measured or inferred from cytosolic Ca^{2+} measurements during sparks (Launikonis et al., 2006b), or twitches (Rudolf et al., 2006; Pape et al., 1995; Launikonis et al., 2006b), was at most 17%, but probably substantially less, especially in the case of sparks, thus completing the evidence that depletion does not play a terminating role in physiological Ca^{2+} release.

On the other hand there is much evidence in favor of Ca^{2+}-dependent inactivation as a mechanism of termination of cell-wide Ca^{2+} release (first suggested by Baylor et al., 1983; Melzer et al., 1984). This includes the increase in release permeability associated with the presence of a Ca^{2+} chelator (Baylor and Hollingworth, 1988; Jong et al., 1993), the relationship between Ca^{2+} release recovery and decay of $[Ca^{2+}]$ in the cytosol (Schneider and Simon, 1988), and the effects of SR depletion on release permeability (Jong et al., 1995; Pape et al., 1995, 1998; Pape and Carrier, 1998; Pizarro and Ríos, 2004). It is believed that this inactivation reflects binding to a low affinity "I" site, which keeps the release channel shut when either Ca^{2+} or Mg^{2+} are bound (Meissner, 1994; Laver et al.,1997). Because such inhibition works regardless of the occupancy of the activation site, the effect is adequately classified as an inactivation.

The successful model embodied in Scheme 1 and Eqs. 3–6 could in principle be used to derive germane information, like geometry and binding affinity of the inactivation site. For this purpose the model should be refined to include geometric features of the spark source, as was done for example by Pape et al. (1998) to interpret the effects of partial SR calcium depletion. This geometry, however, will necessarily be complex, due to the coexistence of junctional and parajunctional channels (Felder and Franzini-Armstrong, 2002) facing cytosolic regions with different constraints to diffusion and different Ca^{2+} transport devices. The success of the extremely simplified model presented here, together with the absence of other good candidates, suggest that CDI is the chief mechanism of release termination in Ca^{2+} sparks. The kinetic similarities with cell-wide Ca^{2+} release illustrated by Fig. 1 indicate that mechanisms operative at the level of sparks also determine the evolution of cell-wide signals. The present considerations are strictly valid for amphibian muscle. Mammalian muscle, in which Ca^{2+} sparks (and CICR) do not play a similar role (e.g., Shirokova et al., 1996, 1998; Lamb et al., 2001), still has a powerful mechanism of spontaneous termination (with kinetics similar to that of amphibians, as illustrated by Baylor, 2005). CDI may play a crucial role in this termination as well.

A Plausible Explanation of the Effects of Sulfate

The CDI model can be used to interpret some of the effects of sulfate on spark morphology. Sulfate increases the width of sparks and slightly reduces their amplitude (Zhou et al., 2005). Because its calcium salt has low solubility, it may precipitate with Ca^{2+} inside the SR and lower $[Ca^{2+}]_{SR}$. This effect, however, is unlikely to explain the change in spark morphology, given the weak dependence of spark parameters on $[Ca^{2+}]_{SR}$ (Launikonis et al., 2006a). More probably, the changes in sparks are due to the cytosolic buffer action of sulfate. We showed with Fig. 1 D that sulfate causes T_p, the rise time of maximum amplitude, to shift to higher values. In the framework of model 2, this amounts to prolonging the channel open time at maximum release current, i.e., delaying inactivation. This combination of promotion of activation (by delaying inactivation) and reduction of local $[Ca^{2+}]$ is consistent with other features of the effects unexplained heretofore, including spatial widening of sparks with reduction in their amplitude (Zhou et al., 2005) and the frequent occurrence of events that propagate over distances of several micrometers.

Ca^{2+} Release Termination in Skeletal and Cardiac Muscle

Studies of cardiac muscle in which SR calcium content is modified by extrinsic or intrinsic buffers (e.g., Terentyev et al., 2002, 2003) support a picture of release termination based largely on Ca^{2+} depletion, with additional contributions from an inactivation process (for review see Stern and Cheng, 2004; see also Sobie et al., 2005). It is surprising that Ca^{2+} release termination is slower (giving rise to sparks of longer rise times) in cardiac muscle, where it relies on at least two cooperative mechanisms, than in skeletal muscle, where termination appears to rely on CDI but not depletion. One possible

reason for the greater terminating efficiency of CDI in skeletal muscle is that it makes use of a higher local [Ca^{2+}]. However, no specific comparisons have been reported of spark intensity in cardiac vs. skeletal muscle. Another reason may be a lower susceptibility of the cardiac RyR isoform to inhibition by cis [Ca^{2+}] (which is observed in bilayer experiments, e.g., Fill and Copello, 2002). If it applied to the millisecond time scale reactions in vivo, this difference could justify the need to rely on depletion in heart muscle. Perhaps to enhance the role of depletion, cardiac muscle has evolved a structure with stores of smaller size and Ca^{2+} capacity (e.g., Brochet et al., 2005). Such depletion-centered regulation, which allows cardiomyocytes to function without a strong Ca^{2+}-dependent inactivation, may be an advantage for cells that require Ca^{2+} transients of longer duration than fast twitch skeletal muscle.

A kernel of the present results is that release flux and its duration in Ca^{2+} sparks are (roughly) inversely related. Consequently, their product, that is, the total Ca^{2+} released, is (roughly) constant. That simple CDI models account for this relationship stresses a teleological advantage of CDI; it will keep constant the amount of released Ca^{2+} under varying loads. This insight was first provided by Jong et al. (1993), who showed that channels undergoing CDI could under specific assumptions "count" the ions that they allowed to pass, and Posterino and Lamb (2003), who observed that Ca^{2+} released by an action potential remained constant within a range of SR loads. By contrast, in cardiac muscle Ca^{2+} release appears controlled by what is left in the SR. The advantages of these different regulatory schemes to serve their respective functional needs are yet to be elucidated. In a first approximation, the skeletal muscle approach appears more suited to fulfil the immediate demands of force or speed, regardless of the state in which it leaves the store, while that of cardiac muscle could lead to greater longer term stability of beat strength.

In conclusion, termination of Ca^{2+} release in amphibian skeletal muscles appears to depend on an efficient Ca^{2+}-dependent inactivation, the details of which cannot be elucidated without a better definition of the geometry and channel composition of the source of Ca^{2+} sparks. Mammalian skeletal muscle probably shares these termination mechanisms, which are much more developed than those of cardiac muscle.

APPENDIX

Off-focus Error, Computed with Simulated Sparks

The goal of this appendix is to test the theory of confocal line scanning (Ríos et al., 2001) by means of spark simulations. This theory provides the relationship between distribution of observed (scanned) amplitudes and in-focus (or "true") amplitudes, through Eq. 10.

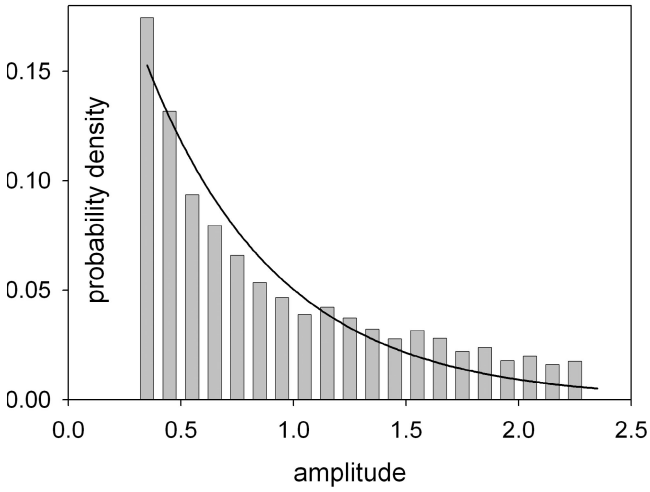

Figure A1. A fundamental property of measured spark amplitudes. Histogram $f(a_s)$ of scanned amplitudes, a_s, for 10,720 sparks simulated with 30 pA current and 5 ms release duration, placed at random y and z distances from the scanning line. Line plots best fit by the inverse function (Eq. 10). Similar deviations between f and fit were observed in simulations with other parameter values.

This relationship can then be inverted under simplifying assumptions to derive in general the distribution of spark amplitude $g(a)$ from the histogram of measured amplitudes $f(a)$. The operator, Eq. 6 of Ríos et al. (2001), is the following:

$$\sigma^2(a)g(a) \propto \frac{d\left[af(a)\right]}{da}, \tag{A1}$$

where σ is the standard deviation of the observed amplitude as a function (assumed isotropic) of displacement from the scanned line.

As argued above, Eq. 10 directly provides a measure of the variance in a due to the random placement of spark sources relative to the line of scanning (because the sole source of variance contemplated by the equation is the placement of the source). Therefore a favorable testing of the theory will confirm the estimate of variance derived from the theory (Eq. 12).

A second goal is to provide a direct estimate of this variance, which can be derived from the simulated sparks whether the simulation supports the theory or not.

A test of Eq. 10 is illustrated in Fig. A1. 10,720 sparks were simulated assuming the same current, 30 pA, and release duration Ξ, 5 ms, placed at random y and z distances from the scanning line. Fig. A1 displays the histogram $f(a)$ of observed amplitudes for the 4,501 events with $a > 0.3$. The continuous line is the best fit by Eq. 10. Clearly, the inverse function provides only a rough approximation to the distribution of scanned amplitude. A deviation was expected because neither the spark nor the PSF are truly Gaussian functions of y and z as required by the theory.

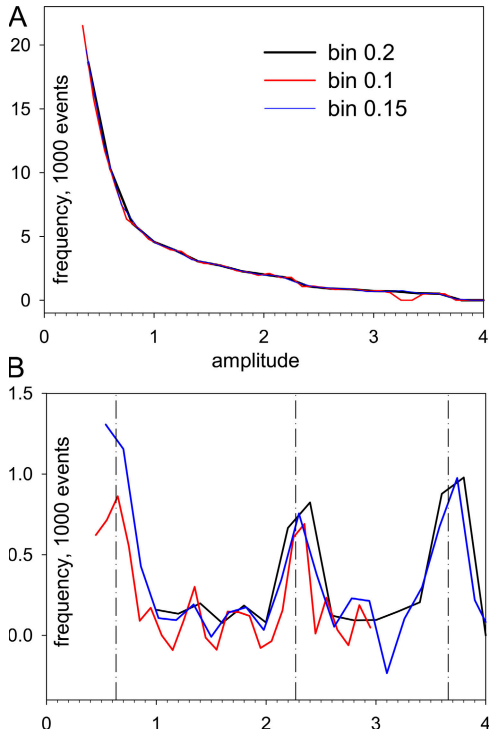

Figure A2. Recovery of "true amplitudes" from distributions of scanned amplitudes. (A) Histograms $f(a_s)$ of scanned amplitudes for a set of sparks consisting in three groups with equal numbers, simulated using three values of current (5, 20, and 50 pA) at three durations (5, 10, and 20 ms). Three alternative binning intervals were used, as indicated. The distribution of true amplitudes in the simulation consists therefore of three Dirac deltas (see below). (B) Distributions $g(a)$ of true amplitudes, derived from $f(a_s)$ in A using Eq. A1. Dashed lines mark the position of true (in-focus) amplitudes of simulated sparks, 0.634, 2.27, and 3.66. Narrow binning is best at locating low amplitude modes and vice versa.

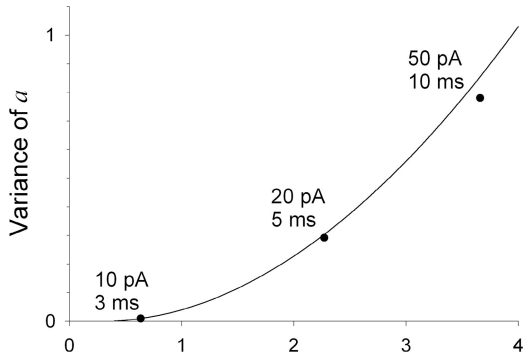

Figure A3. The amplitude variance due to off-focus spread of spark locations. Circles plot variance of scanned amplitude vs. in-focus amplitude for the three groups of simulated sparks represented in Fig. A2. The curve plots variance vs. true amplitude α, calculated by Eq. 12.

The next simulation was designed to test the evaluation of true amplitudes provided by Eq. A1. 32,160 sparks were simulated using three values of current (5, 20, and 50 pA) with Ξ = 5, 10, and 20 ms, respectively. The distribution was therefore concentrated at three values of true amplitude. Among all sparks, 12,134 yielded scanned amplitudes above the detection threshold (0.3). These were then processed to derive $g(a)$. $f(a)$ was computed for three binning intervals, yielding curves represented in Fig. A2 A. Application to these functions of Eq. A1 yielded three versions of $\sigma^2(a)$ $g(a)$ represented with the same color code in Fig. 8 B. These curves have three modes at ~0.6, 2.3, and 3.7, which are very close to the actual in-focus amplitudes of the three sparks, marked with vertical lines in Fig. 8 B. While the frequencies of the three sparks were exactly the same in the simulation, the third mode of g is somewhat higher. This difference may reflect a greater σ (which tends to increase at longer release times) or the fact that a greater fraction of greater sparks will satisfy the detection criterion ($a > 0.3$). The result also depends to some extent on the binning interval (a finer interval resolves small size sparks better, but becomes inadequate as a increases and f decreases). In spite of these inaccuracies, the simulations support the algorithm represented by Eq. A1 as a suitable tool to derive true amplitude distributions (i.e., correct the off-focus error).

The calculation of variance due to off-focus error, based on this theory of line scanning, was also tested with simulations. The continuous curve in Fig. A3 represents the variance of scanned amplitude of sparks, calculated using Eq. 12, against their in-focus amplitude. The symbols represent the variance for the three sets of sparks in Fig. 8. Again, the simulations demonstrate the predictive value of the theory. On this basis, and as stated in the text, an estimate of 0.285 is reached for the component of the variance due to off-focus error.

That scanned amplitude is the least robust of the morphometric parameters of sparks has been recognized since early on in their study (e.g., Pratusevich and Balke, 1996). Our theory of confocal scanning, supported by the present simulations, provides a quantitative measure of this variability. The contribution of the off -focus displacements to the variance in spark amplitude is 80–90%. Given this strikingly high value, even small changes in observed amplitude associated with any intervention or spark parameter may have mechanistic significance. The quantitative estimate embodied by Eq. 12 provides a tool to appraise the relevance of such changes.

We are grateful to Sandrine Pouvreau, Leandro Royer, and Demetrio Santiago (Rush University) for careful editing and insightful suggestions on the manuscript.

This work was supported by grants of the National Institutes of Arthritis and Musculoskeletal and Skin Disease, National Institutes of Health (to E. Ríos), and Programa Educacional de Desarrollo de las Ciencias Básicas, Uruguay, to G. Brum. B.S. Launikonis was the recipient of a C.J. Martin Fellow of the National Medical Research Council of Australia.

Olaf S. Andersen served as editor.

Submitted: 9 August 2007
Accepted: 28 February 2008

REFERENCES

Baylor, S.M. 2005. Calcium sparks in skeletal muscle fibers. *Cell Calcium.* 37:513–530.

Baylor, S.M., and S. Hollingworth. 1988. Fura-2 calcium transients in frog skeletal muscle fibres. *J. Physiol.* 403:151–192.

Baylor, S.M., W.K. Chandler, and M.W. Marshall. 1983. Sarcoplasmic reticulum calcium release in frog skeletal muscle fibres estimated from Arsenazo III calcium transients. *J. Physiol.* 344:625–666.

Beard, N.A., M.M. Sakowska, A.F. Dulhunty, and D.R. Laver. 2002. Calsequestrin is an inhibitor of skeletal muscle ryanodine receptor calcium release channels. *Biophys. J.* 82:310–320.

Beard, N.A., M.G. Casarotto, L. Wei, M. Varsanyi, D.R. Laver, and A.F. Dulhunty. 2005. Regulation of ryanodine receptors by calsequestrin: effect of high luminal Ca^{2+} and phosphorylation. *Biophys. J.* 88:3444–3454.

Blatter, L.A., J. Huser, and E. Ríos. 1997. Sarcoplasmic reticulum Ca^{2+} release flux underlying Ca^{2+} sparks in cardiac muscle. *Proc. Natl. Acad. Sci. USA.* 94:4176–4181.

Brochet, D.X., D. Yang, A. Di Maio, W.J. Lederer, C. Franzini-Armstrong, and H. Cheng. 2005. Ca^{2+} blinks: rapid nanoscopic store calcium signaling. *Proc. Natl. Acad. Sci. USA.* 102:3099–3104.

Brum, G., N. Piriz, R. DeArmas, E. Rios, M. Stern, and G. Pizarro. 2003. Differential effects of voltage-dependent inactivation and local anaesthetics on kinetic phases of Ca^{2+} release in frog skeletal muscle. *Biophys. J.* 85:245–254.

Chandler, W.K., S. Hollingworth, and S.M. Baylor. 2003. Simulation of calcium sparks in cut skeletal muscle fibers of the frog. *J. Gen. Physiol.* 121:311–324.

Felder, E., and C. Franzini-Armstrong. 2002. Type 3 ryanodine receptors of skeletal muscle are segregated in a parajunctional position. *Proc. Natl. Acad. Sci. USA.* 99:1695–1700.

Fill, M., and J.A. Copello. 2002. Ryanodine receptor calcium release channels. *Physiol. Rev.* 82:893–922.

Franzini-Armstrong, C., F. Protasi, and V. Ramesh. 1999. Shape, size, and distribution of Ca^{2+} release units and couplons in skeletal and cardiac muscles. *Biophys. J.* 77:1528–1539.

González, A., W.G. Kirsch, N. Shirokova, G. Pizarro, M.D. Stern, and E. Ríos. 2000. The spark and its ember: separately gated local components of Ca^{2+} release in skeletal muscle. *J. Gen. Physiol.* 115:139–158.

Györke, S., I. Györke, V. Lukyanenko, D. Terentyev, S. Viatchenko-Karpinski, and T.F. Wiesner. 2002. Regulation of sarcoplasmic reticulum calcium release by luminal calcium in cardiac muscle. *Front. Biosci.* 7:d1454–d1463.

Jacquemond, V., L. Csernoch, M.G. Klein, and M.F. Schneider. 1991. Voltage-gated and calcium-gated calcium release during depolarization of skeletal muscle fibers. *Biophys. J.* 60:867–873.

Jiang, Y.H., M.G. Klein, and M.F. Schneider. 1999. Numerical simulation of Ca^{2+} "Sparks" in skeletal muscle. *Biophys. J.* 77:2333–2357.

Jong, D.S., P.C. Pape, W.K. Chandler, and S.M. Baylor. 1993. Reduction of calcium inactivation of sarcoplasmic reticulum calcium release by fura-2 in voltage clamped cut twitch fibers from frog muscle. *J. Gen. Physiol.* 102:333–370.

Jong, D.S., P.C. Pape, S.M. Baylor, and W.K. Chandler. 1995. Calcium inactivation of calcium release in frog cut muscle fibers that contain millimolar EGTA or Fura-2. *J. Gen. Physiol.* 106:337–388.

Kettlun, C., A. González, E. Ríos, and M. Fill. 2003. Unitary Ca^{2+} current through mammalian cardiac and amphibian skeletal muscle ryanodine receptor channels under near-physiological ionic conditions. *J. Gen. Physiol.* 122:407–417.

Klein, M.G., and M.F. Schneider. 2006. Ca^{2+} sparks in skeletal muscle. *Prog. Biophys. Mol. Biol.* 92:308–332.

Klein, M.G., H. Cheng, L.F. Santana, Y.H. Jiang, W.J. Lederer, and M.F. Schneider. 1996. Two mechanisms of quantized calcium release in skeletal muscle. *Nature.* 379:455–458.

Klein, M.G., A. Lacampagne, and M.F. Schneider. 1997. Voltage dependence of the pattern and frequency of discrete Ca^{2+} release events after brief repriming in frog skeletal muscle. *Proc. Natl. Acad. Sci. USA.* 94:11061–11066.

Lacampagne, A., C.W. Ward, M.G. Klein, and M.F. Schneider. 1999. Time course of individual Ca^{2+} sparks in frog skeletal muscle recorded at high time resolution. *J. Gen. Physiol.* 113:187–198.

Lacampagne, A., M.G. Klein, C.W. Ward, and M.F. Schneider. 2000. Two mechanisms for termination of individual Ca^{2+} sparks in skeletal muscle. *Proc. Natl. Acad. Sci. USA.* 97:7823–7828.

Lamb, G.D., M.A. Cellini, and D.G. Stephenson. 2001. Different Ca^{2+} releasing action of caffeine and depolarisation in skeletal muscle fibres of the rat. *J. Physiol.* 531:715–728.

Launikonis, B.S., J. Zhou, D. Santiago, G. Brum, and E. Ríos. 2006a. The changes in Ca^{2+} sparks associated with measured modifications of intra-store Ca^{2+} concentration in skeletal muscle. *J. Gen. Physiol.* 128:45–54.

Launikonis, B.S., J. Zhou, L. Royer, T.R. Shannon, G. Brum, and E. Ríos. 2006b. Depletion "skraps" and dynamic buffering inside the cellular calcium store. *Proc. Natl. Acad. Sci. USA.* 103:2982–2987.

Laver, D.R., T.M. Baynes, and A.F. Dulhunty. 1997. Magnesium inhibition of ryanodine-receptor calcium channels: evidence for two independent mechanisms. *J. Membr. Biol.* 156:213–229.

Meissner, G. 1994. Ryanodine receptor/Ca^{2+} release channels and their regulation by endogenous effectors. *Annu. Rev. Physiol.* 56:485–508.

Melzer, W., E. Ríos, and M.F. Schneider. 1984. Time course of calcium release and removal in skeletal muscle fibers. *Biophys. J.* 45:637–641.

Pape, P.C., and N. Carrier. 1998. Effect of sarcoplasmic reticulum (SR) calcium content on SR calcium release elicited by small voltage-clamp depolarizations in frog cut skeletal muscle fibers equilibrated with 20 mM EGTA. *J. Gen. Physiol.* 112:161–179.

Pape, P.C., D.S. Jong, W.K. Chandler, and S.M. Baylor. 1993. Effect of fura-2 on action potential-stimulated calcium release in cut twitch fibers from frog muscle. *J. Gen. Physiol.* 102:295–332.

Pape, P.C., D.S. Jong, and W.K. Chandler. 1995. Calcium release and its voltage dependence in frog cut muscle fibers equilibrated with 20 mM EGTA. *J. Gen. Physiol.* 106:259–336.

Pape, P.C., D.S. Jong, and W.K. Chandler. 1998. Effects of partial sarcoplasmic reticulum calcium depletion on calcium release in frog cut muscle fibers equilibrated with 20 mM EGTA. *J. Gen. Physiol.* 112:263–295.

Pape, P.C., K. Fénelon, and N. Carrier. 2002. Extra activation component of calcium release in frog muscle fibres. *J. Physiol.* 542:867–886.

Pizarro, G., and E. Ríos. 2004. How source content determines intracellular Ca^{2+} release kinetics. Simultaneous measurement of [Ca^{2+}] transients and [H^+] displacement in skeletal muscle. *J. Gen. Physiol.* 124:239–258.

Pizarro, G., L. Csernoch, I. Uribe, and E. Ríos. 1992. Differential effects of tetracaine on two kinetic components of calcium release in frog skeletal muscle fibres. *J. Physiol.* 457:525–538.

Posterino, G.S., and G.D. Lamb. 2003. Effect of sarcoplasmic reticulum Ca^{2+} content on action potential-induced Ca^{2+} release in rat skeletal muscle fibres. *J. Physiol.* 551:219–237.

Pouvreau, S., L. Royer, J. Yi, G. Brum, G. Meissner, E. Ríos, and J. Zhou. 2007. Ca^{2+} sparks operated by membrane depolarization require isoform 3 ryanodine receptor channels in skeletal muscle. *Proc. Natl. Acad. Sci. USA.* 104:5235–5240.

Pratusevich, V.R., and C.W. Balke. 1996. Factors shaping the confocal image of the calcium spark in cardiac muscle cells. *Biophys. J.* 71:2942–2957.

Rengifo, J., R. Rosales, A. González, H. Cheng, M.D. Stern, and E. Ríos. 2002. Intracellular Ca^{2+} release as irreversible Markov process. *Biophys. J.* 83:2511–2521.

Ríos, E., and G. Pizarro. 1991. Voltage sensor of excitation-contraction coupling in skeletal muscle. *Physiol. Rev.* 71:849–908.

Ríos, E., M.D. Stern, A. González, G. Pizarro, and N. Shirokova. 1999. Calcium release flux underlying Ca^{2+} sparks of frog skeletal muscle. *J. Gen. Physiol.* 114:31–48.

Ríos, E., N. Shirokova, W.G. Kirsch, G. Pizarro, M.D. Stern, H. Cheng, and A. González. 2001. A preferred amplitude of calcium sparks in skeletal muscle. *Biophys. J.* 80:169–183.

Ríos, E., B.S. Launikonis, L. Royer, G. Brum, and J. Zhou. 2006. The elusive role of store depletion in the control of intracellular calcium release. *J. Muscle Res. Cell Motil.* 27:337–350.

Rome, L.C., D.A. Syme, S. Hollingworth, S.L. Lindstedt, and S.M. Baylor. 1996. The whistle and the rattle: the design of sound producing muscles. *Proc. Natl. Acad. Sci. USA.* 93:8095–8100.

Rudolf, R., P.J. Magalhaes, and T. Pozzan. 2006. Direct in vivo monitoring of sarcoplasmic reticulum Ca^{2+} and cytosolic cAMP dynamics in mouse skeletal muscle. *J. Cell Biol.* 173:187–193.

Schneider, M.F., and B.J. Simon. 1988. Inactivation of calcium release from the sarcoplasmic reticulum in frog skeletal muscle. *J. Physiol.* 405:727–745.

Shirokova, N., J. García, G. Pizarro, and E. Ríos. 1996. Ca^{2+} release from the sarcoplasmic reticulum compared in amphibian and mammalian skeletal muscle. *J. Gen. Physiol.* 107:1–18.

Shirokova, N., J. García, and E. Ríos. 1998. Local calcium release in mammalian skeletal muscle. *J. Physiol.* 512:377–384.

Sobie, E.A., L.S. Song, and W.J. Lederer. 2005. Local recovery of Ca^{2+} release in rat ventricular myocytes. *J. Physiol.* 565:441–447.

Stern, M.D., and H. Cheng. 2004. Putting out the fire: what terminates calcium-induced calcium release in cardiac muscle? *Cell Calcium.* 35:591–601.

Stern, M.D., G. Pizarro, and E. Ríos. 1997. Local control model of excitation-contraction coupling in skeletal muscle. *J. Gen. Physiol.* 110:415–440.

Terentyev, D., S. Viatchenko-Karpinski, H.H. Valdivia, A.L. Escobar, and S. Györke. 2002. Luminal Ca^{2+} controls termination and refractory behavior of Ca^{2+}-induced Ca^{2+} release in cardiac myocytes. *Circ. Res.* 91:414–420.

Terentyev, D., S. Viatchenko-Karpinski, I. Györke, P. Volpe, S.C. Williams, and S. Györke. 2003. Calsequestrin determines the functional size and stability of cardiac intracellular calcium stores: mechanism for hereditary arrhythmia. *Proc. Natl. Acad. Sci. USA.* 100:11759–11764.

Wang, S.Q., L.S. Song, L. Xu, G. Meissner, E.G. Lakatta, E. Ríos, M.D. Stern, and H. Cheng. 2002. Thermodynamically irreversible gating of ryanodine receptors in situ revealed by stereotyped duration of release in Ca2+ sparks. *Biophys. J.* 83:242–251.

Wang, S.Q., M.D. Stern, E. Ríos, and H. Cheng. 2004. The quantal nature of Ca^{2+} sparks and in situ operation of the ryanodine receptor array in cardiac cells. *Proc. Natl. Acad. Sci. USA.* 101:3979–3984.

Wei, L., M. Varsanyi, A.F. Dulhunty, and N.A. Beard. 2006. The conformation of calsequestrin determines its ability to regulate skeletal ryanodine receptors. *Biophys. J.* 91:1288–1301.

Zhou, J., G. Brum, A. González, B.S. Launikonis, M.D. Stern, and E. Ríos. 2003. Ca^{2+} sparks and embers of mammalian muscle. Properties of the sources. *J. Gen. Physiol.* 122:95–114.

Zhou, J., G. Brum, A. González, B.S. Launikonis, M.D. Stern, and E. Ríos. 2005. Concerted vs. sequential. Two activation patterns of vast arrays of intracellular Ca^{2+} channels in muscle. *J. Gen. Physiol.* 126:301–309.